Check for updates

NANO · MICRO small
www.small-journal.com

14-Electron Redox Chemistry Enabled by Salen-Based π-Conjugated Framework Polymer Boosting High-Performance Lithium-Ion Storage

Xinlu Zhang, Seyedeh Alieh Kazemi, Xingtao Xu, Jonathan P. Hill, Jiachen Wang, Haibo Li, Saad M. Alshehri, Tansir Ahamad, Yoshio Bando, Yusuke Yamauchi, Yun Wang,* and Likun Pan**

A paucity of redox centers, poor charge transport properties, and low structural stability of organic materials obstruct their use in practical applications. Herein, these issues have been addressed through the use of a redox-active salen-based framework polymer (RSFP) containing multiple redox-active centers in π-conjugated configuration for applications in lithium-ion batteries (LIBs). Based on its unique architecture, RSFP exhibits a superior reversible capacity of 671.8 mAh g^{-1} at 0.05 A g^{-1} after 168 charge-discharge cycles. Importantly, the lithiation/de-lithiation performance is enhanced during operation, leading to an unprecedented reversible capacity of 946.2 mAh g^{-1} after 3500 cycles at 2 A g^{-1}. The structural evolution of RSFP is studied ex situ using X-ray photoelectron spectroscopy, revealing multiple active C═N, C—O, and C═O sites and aromatic sites such as benzene rings. Remarkably, the emergence of C═O originated from C—O is triggered by an electrochemical process, which is beneficial for improving reversible lithiation/delithiation behavior. Furthermore, the respective strong and weak binding interactions between redox centers and lithium ions, corresponding to theoretical capacities of 670.1 and 938.2 mAh g^{-1}, have been identified by density functional theory calculations manifesting 14-electron redox reactions. This work sheds new light on routes for the development of redox-active organic materials for energy storage applications.

1. Introduction

Rechargeable lithium-ion batteries (LIBs) are popular state-of-the-art energy storage devices used widely in consumer electronics, electric vehicles, and wearable electronic devices owing to their high energy density and favorable long-term cycling stability.[1–4] The development of renewable, green electrode materials is critical for the sustainability of LIBs and is driven by various energy and environmental issues including the need to reduce the consumption of nonrenewable fossil fuels.[5–7] Organic electrode materials, which are of low cost and excellent availability from easily accessible environmentally friendly natural sources, have received much attention as promising candidates for the next generation of LIBs.[8,9] Their flexible structural design and scalable synthesis through tailored molecular engineering allow the preparation of organic electrode materials with controllable structural properties, including tunable redox centers, π-conjugated

X. Zhang, J. Wang, L. Pan
Shanghai Key Laboratory of Magnetic Resonance
School of Physics and Electronic Science
East China Normal University
Shanghai 200241, China
E-mail: lkpan@phy.ecnu.edu.cn
S. A. Kazemi, Y. Wang
Centre for Catalysis and Clean Energy
School of Environment and Science
Gold Coast Campus
Griffith University
Southport 4222, Australia
E-mail: yun.wang@griffith.edu.au
The ORCID identification number(s) for the author(s) of this article can be found under https://doi.org/10.1002/smll.202309321

© 2024 The Authors. Small published by Wiley-VCH GmbH. This is an open access article under the terms of the Creative Commons Attribution License, which permits use, distribution and reproduction in any medium, provided the original work is properly cited.

DOI: 10.1002/smll.202309321

X. Xu
Marine Science and Technology Collage
Zhejiang Ocean University
Zhoushan 316022, China
E-mail: xingtao.xu@zjou.edu.cn
J. P. Hill, Y. Bando
Research Center for Materials Nanoarchitectonics (MANA)
National Institute for Materials Science (NIMS)
1-1 Namiki, Tsukuba, Ibaraki 305-0044, Japan
H. Li
Ningxia Key Laboratory of Photovoltaic Materials
Ningxia University
Yinchuan, Ningxia 750021, China
S. M. Alshehri, T. Ahamad, Y. Bando
Chemistry Department
College of Science
King Saud University
P.O. Box 2455, Riyadh 11451, Saudi Arabia

frameworks, lithiation/de-lithiation voltage plateaus, electrochemical stability, and optimum diffusion kinetics.[10,11] For this reason, tremendous effort has been devoted to the design of sustainable electrode materials for LIBs, including organic free radicals, conjugated carbonyls, and organosulfur and organic carbon/nitrogen compounds.[12,13] Unfortunately, these organic electrode materials are generally of low structural stability resulting from their high solubility in organic electrolytes, which impedes the large-scale application of organic materials in LIBs.[14,15] Considering these aspects, it is critical to improve the stability of organic electrode materials so that they can be applied as low-cost, environmentally friendly, and sustainable electrode materials.

Organic framework polymers with unique configurations have received increasing interest as promising organic electrode materials for LIBs based on their abundant pore apertures, which facilitate lithium-ion diffusion in organic electrolytes, and their large surface areas, which improve the contact area between the electrode and lithium ions.[16,17] Frameworks constructed by directly polymerizing functional organic building blocks involve strong covalent linkages and inhibit the dissolution of electrode materials in organic electrolytes.[18] However, the polymerization of organic building blocks usually yields materials having poor electron transfer properties, and suppresses the volumetric energy density due to the lack of redox centers and low theoretical capacity.[19] This poor electrical conductivity of organic polymers might be overcome by the construction of π-conjugated organic frameworks.[20] Such π-conjugated frameworks could improve electron transport and accommodate lithium ions to form Li_6/C_6, leading to extremely high theoretical capacities of up to 2200 mAh g^{-1}.[21] Apart from the potential contribution of each benzene ring, which can accommodate up to six lithium ions, redox reactions involving lithium ions and other organic functional groups are increasingly likely to occur. Functional groups containing electron lone pairs, including N- and O- containing C=N, C—O, and C=O groups, are responsible for the superior storage capacity and high volumetric energy densities of the known organic electrode materials.[22–24] Although extensive research has focused on the development of organic framework polymers with redox activity,[8,24–26] conjugated frameworks with accessible active sites are seldom selected as anodes for LIBs because of the lack of suitable redox-active species as building blocks. Therefore, it has been a significant challenge to develop conjugated organic frameworks with redox-active sites for use as high-performance anode materials in sustainable LIBs.

Y. Yamauchi
Department of Materials Process Engineering
Graduate School of Engineering
Nagoya University, Nagoya University
Nagoya 464–8601, Japan
Y. Yamauchi
Australian Institute for Bioengineering and Nanotechnology (AIBN)
School of Chemical Engineering
The University of Queensland
Brisbane, QLD 4072, Australia
Y. Yamauchi
Department of Chemical and Biomolecular Engineering
Yonsei University
50 Yonsei-ro, Seodaemun-gu, Seoul 03722, South Korea

In this work, we report a redox-active salen-based framework polymer (RSFP) containing multiple redox species and a π-conjugated organic framework as an efficient organic anode for LIBs. RSFP materials possess several advantages: 1) multiple accessible redox centers act as binding sites for lithium ions; 2) the π-conjugated organic framework accelerates electron transport; 3) the polymerized organic skeleton linked with strong imine bonds improves structural stability; 4) a well-defined pore aperture facilitates lithium-ion diffusion in the organic electrolyte; 5) the large surface area improves contact between the active electrode and electrolyte; and 6) the unique architecture shortens lithium-ion diffusion distances. Thus, RSFP exhibits a superior reversible capacity of 671.8 mAh g^{-1} after 168 cycles at 0.05 A g^{-1} and a robust rate capacity of 138.6 mAh g^{-1} at 4 A g^{-1}. More importantly, the lithium-ion insertion/extraction performance is enhanced during operation, leading to an unprecedented storage capacity of 946.2 mAh g^{-1} after 3500 cycles at 2 A g^{-1}. The structural evolution of RSFP during the lithiation/de-lithiation process was studied ex situ using X-ray photoelectron spectroscopy (XPS), indicating the presence of multiple active C=N, C—O, and C=O sites along with benzene rings in the organic framework. Remarkably, the transformation of C—O into C=O in the organic framework of RSFP was triggered by an electrochemical process, which is beneficial for enhancing the reversible electrochemical performance. Moreover, the strong and weak binding interactions between redox centers and lithium ions correspond respectively to theoretical capacities of 670.1 and 938.2 mAh g^{-1}, and were demonstrated to involve 14-electron redox processes by using density functional theory (DFT) calculations.

2. Results and Discussion

Figure 1a shows the synthetic route of RSFP, which involves a Schiff-base polymerization reaction between two organic building blocks, namely, 2,5-dihydroxy-1,4-benzenedicarboxaldehyde (HBC) and 1,2,4,5-benzenetetraamine tetrahydrochloride (BTA), under anhydrous conditions with trace acetic acid as catalyst through the formation of imine bonds as covalent organic linkers. The resulting polymer has a π-conjugated organic framework with different chemical bonds (Figure S1, Supporting Information). Four-point probe measurements reveal an excellent electrical conductivity (1.304×10^{-6} S m^{-1}), which is favorable for accelerating electron transport. The RSFP also combines the structural features of the salen groups with multiple available nitrogen and oxygen atoms.[27,28] As shown in Figures 1b,c, the periodic RSFP framework has ordered pores in its 2D layered structure that was identified previously. The organic framework of RSFP was characterized by ^{13}C solid-state nuclear magnetic resonance (NMR) spectroscopy. The NMR spectrum in Figure 1d contains two distinct signals at 150 and 57.6 ppm ascribed to C=N and C—N, respectively,[30,31] indicating successful polymerization between BTA and HBC. In addition, three broad signals in the chemical shift ranges of 95–100.6, 115–119, and 128–133 ppm[32,33] along with a weak signal at 140 ppm are assigned to aromatic carbons in the organic framework,[34] while the characteristic signal at 177 ppm corresponds to the carbon bonded to the hydroxyl groups in RSFP.[24] It should be noted that the peaks found in the chemical shift range of 10–50 ppm correspond to

© 2024 The Authors. Small published by Wiley-VCH GmbH

16136829, 2024, 28, Downloaded from https://onlinelibrary.wiley.com/doi/10.1002/smll.202309321 by National Institute For, Wiley Online Library on [12/11/2024]. See the Terms and Conditions (https://onlinelibrary.wiley.com/terms-and-conditions) on Wiley Online Library for rules of use; OA articles are governed by the applicable Creative Commons License

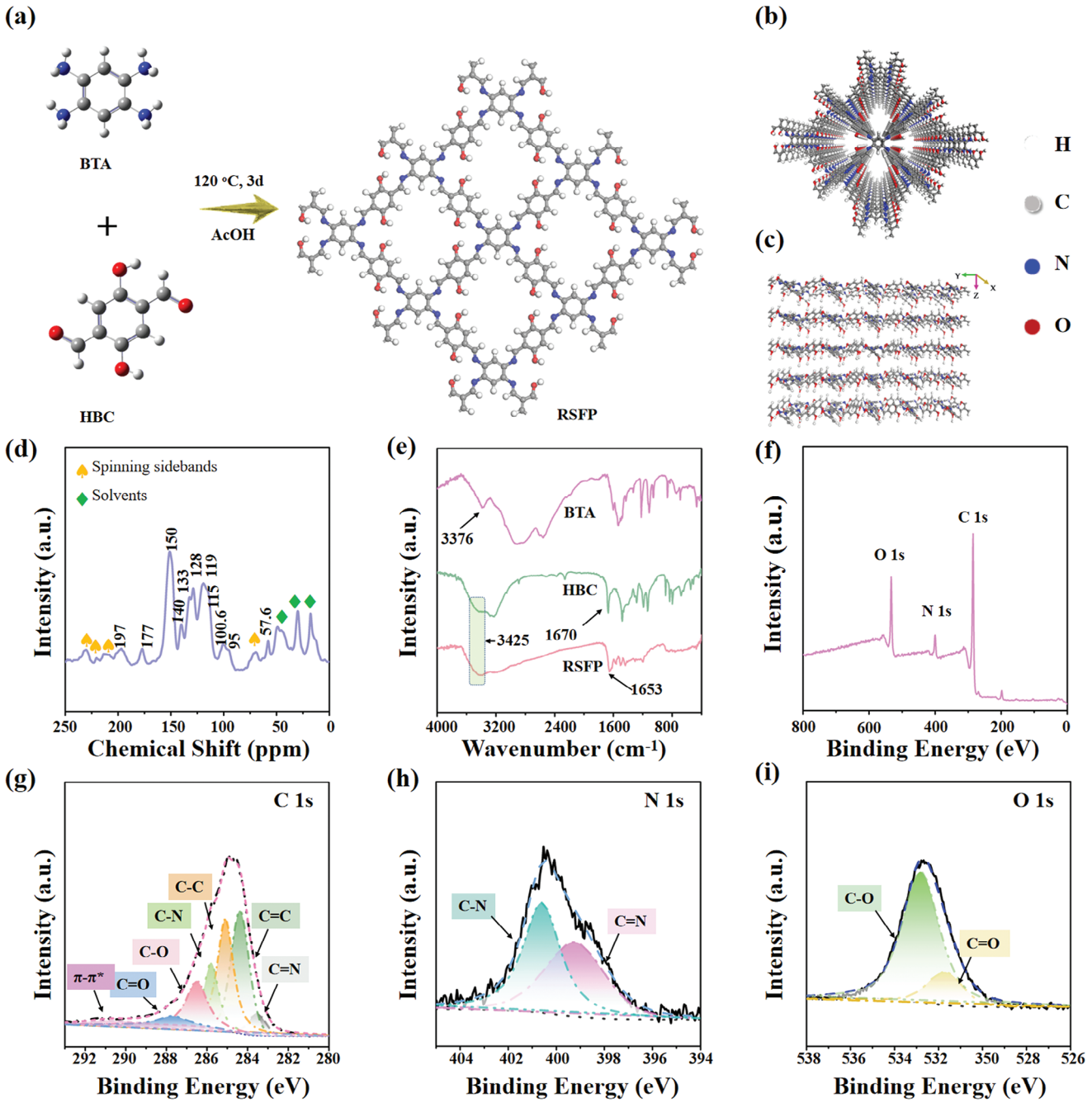

Figure 1. a) Schematic illustration of the synthetic process. Top (b) and (c) side views of RSFP (H, white; C, gray; N, blue; O, red). d) 13C solid-state NMR spectrum of RSFP. e) Fourier-transform infrared (FT-IR) spectra of BTA, HBC, and RSFP. f) XPS survey spectrum, g) C 1s, h) N 1s, and i) O 1s high-resolution XPS spectra of RSFP.

solvents in the pore channels of RSFP.[28,35] The weak peak at 197 ppm, which is due to C═O,[32,36] indicates the presence of traces of unreacted terminal aldehyde in the organic skeleton of RSFP in agreement with previous reports.[26]

The chemical groups present in RSFP were investigated by FT-IR spectroscopy. As shown in Figure 1e, a stretching vibration band at 1653 cm^{-1} in the spectrum of RSFP is assigned to C═N in the organic framework of RSFP. The two adsorption bands at 3376 and 1670 cm^{-1} in the spectra of the starting materials are respectively assigned to the stretching vibration bands of $-NH_2$ in BTA and C═O in HBC. These are absent from the spectrum of RSFP, confirming the successful condensation reaction between BTA and HBC.[27] Furthermore, a broad adsorption peak at 3425 cm^{-1} is assigned to the stretching vibration of —OH groups in the organic skeleton of RSFP, suggesting the presence of salen groups.[31] To further study the covalent bonding and chemical environment of RSFP, XPS measurements were performed (Figure 1f–i). The main elements in RSFP are C, N, and

© 2024 The Authors. Small published by Wiley-VCH GmbH

16136829, 2024, 28, Downloaded from https://onlinelibrary.wiley.com/doi/10.1002/smll.202309321 by National Institute For, Wiley Online Library on [12/11/2024]. See the Terms and Conditions (https://onlinelibrary.wiley.com/terms-and-conditions) on Wiley Online Library for rules of use; OA articles are governed by the applicable Creative Commons License

O, as revealed by the XPS survey spectrum (Figure 1f). As shown in Figure 1g, the high-resolution C 1s XPS spectrum can be deconvoluted into five distinct peaks at 283.52, 284.36, 285.13, 286, and 286.95 eV, which can be attributed to C═N, C═C, C—C, C—N, and C—O, respectively.[8,26] Notably, a small peak at 288.0 eV is assigned to unreacted terminal aldehyde groups in the organic framework of RSFP,[26] consistent with the weak C═O signal at 197 ppm in the solid-state NMR spectrum (Figure 1d). A broad peak at 290.93 eV is assigned to the π–π* stacking interactions between organic layers, which is also consistent with previous reports.[37] These interactions facilitate lithium-ion diffusion to improve the electrochemical performance. The N 1s spectrum in Figure 1h can be deconvoluted to two peaks at 397.9 and 399.2 eV, respectively corresponding to C═N and C—N, which implies the formation of imine-based linkers.[38] Figure 1i shows the high-resolution O 1s spectrum deconvoluted into two peaks at 530.75 and 531.74 eV, respectively corresponding to C═O and C—O, consistent with the NMR result.

The crystallinity of RSFP was investigated by X-ray diffraction (XRD, Figure S2, Supporting Information). The XRD pattern of RSFP exhibits a strong diffraction peak at $2\theta = 1.26^{\circ}$ located in the small-angle diffraction region, indicating the long-range molecular ordering of the organic framework (Figure S2b, Supporting Information).[39] Moreover, a diffraction peak at ≈25.2° corresponds to the presence of the (001) facet resulting from the π–π* stacking of organic layers with an interlayer distance of 3.53 Å calculated according to the Bragg equation.[27] This is beneficial for lithium-ion diffusion in organic electrolyte, further improving the electrochemical performance.[40] In addition, a broad peak at $\approx 2\theta = 5°$–45° and some other weak diffraction peaks can be ascribed to a combination of a small crystalline domains and an amorphous phase. To further understand the crystalline structure, the crystallographic parameters of RSFP were obtained based on a Pawley refinement despite the peak intensities being very weak (Table S1, Supporting Information). This gives a unit cell with a P1 (C1-1) space group and dimensions $a = 13.17$ Å, $b = 13.17$ Å, $c = 3.60$ Å, $\alpha = 89.97°$, $\beta = 90.00°$, and $\gamma = 81.72°$. Moreover, the weak diffraction peaks at $2\theta = 8.9°$, 10.5°, 14.6° and 18.1° (Figure S2c, Supporting Information) were assigned the (110), (020), (031), and (040) planes based on the slipped stacking model of RSFP in accordance with the previous report.[27]

The thermal stability of RSFP was investigated by thermogravimetric analysis (TGA) under a nitrogen atmosphere (Figure S3, Supporting Information). The first weight loss of 10.3% in the temperature range from 30 to 180 °C is ascribed to the loss of solvent molecules from the pores of RSFP due to the different binding forces between the organic framework and various solvent molecules.[6,17] Subsequently, the significant weight loss commencing at 180 °C corresponds to the decomposition of the organic framework to yield a carbon framework and is usually accompanied by the disappearance of organic groups in RSFP.[41] To further verify the structural stability of RSFP, it was soaked in various solvents (Figure S4, Supporting Information) and investigated by FT-IR (Figure S5, Supporting Information), revealing its outstanding structural stability ascribed to the robust covalent bonds of imines.[26] The pore characteristics and specific surface area of RSFP were evaluated by measuring the nitrogen adsorption/desorption isotherms at 77 K (Figure S6, Supporting Information), where a sharp uptake for nitrogen adsorption below $P/P_0 = 0.03$ (inset of Figure S6, Supporting Information) indicates a microporous structure.[31] The pore size distribution was further calculated using a nonlocal DFT model. The main pore signals occur at ≈14, 23, and 37 Å, indicating a mixture of micro- and mesopores (Figure S7, Supporting Information). This pore size distribution is beneficial for lithium-ion diffusion in organic electrolytes. The Brunauer–Emmett–Teller (BET) specific surface area of RSFP is estimated to be 99.4 $m^2\ g^{-1}$ for fitting by the multi-point BET method with a very good R^2 value (Figure S8, Supporting Information), and the total pore volume is 0.287 $cm^3\ g^{-1}$. The low porosity of RSFP is possibly due to the strong interlayer attraction based on π–π* stacking of the conjugated aromatic rings. Notably, the surface area of RSFP synthesized in solution in the absence of a foaming agent is believed to be sufficient for its use as electrode materials because of the large surface area based on unavoidable side reactions and the large consumption of organic electrolyte to form an SEI layer.[29,42] It helps to improve the contact between organic electrolyte and electrochemical lithium storage sites in the organic skeleton as illustrated by a contact angle experiment (Figure S9, Supporting Information) conducted during the charge/discharge process.

The morphology of RSFP was observed by field-emission scanning electron microscopy (FE-SEM). As shown in **Figure 2**a, a uniform coral-like structure with a length of ≈400 nm and a diameter of ≈100 nm was observed. This mosphology helps to effectively shorten the lithium-ion diffusion distance thus improving the electrochemical performance.[19] The detailed microstructure of RSFP was also observed by transmission electron microscopy (TEM). Figure 2b shows the rough surface of RSFP, which also helps to promote the contact between organic electrolyte and electrochemical storage sites in the organic framework. Although some regions are amorphous (Figure 2c), most regions show clear lattice fringes of RSFP, indicating the successful synthesis of RSFP having a polycrystalline structure (Figure 2d). The lattice fringes are randomly oriented and the average crystallite size is very small, which is in accordance with the XRD results in Figure S2c (Supporting Information). The SAED pattern in Figure 2e shows the well-defined diffraction rings with sparse diffraction spots, further confirming the polycrystalline nature of RSFP.[43] It should be noted that d values calculated from the lattice fringes and SAED are not accurate, possibly because the organic frameworks are distorted by the electron beam during TEM observation. The amorphous structure of RSFP decorated with polycrystalline areas is probably due to the incomplete crystallization process.

The lithiation/de-lithiation reaction of RSFP was further evaluated in standard CR2032 coin-type cells containing an organic electrolyte, and demonstrates its excellent structural stability (Figure S10, Supporting Information). To investigate the lithiation/delithiation reaction of RSFP, cyclic voltammetry (CV) was carried out in the voltage range of 0.01–3.0 V. From **Figure 3**a, two broad cathodic peaks at 1.47 and 0.63 V are clearly observed during the initial discharge process. These can be ascribed to the lithiation behavior of phenol and nitrogen atoms as well as C_6 aromatic benzene.[26] The weak peak observed at 1.15 V in the first cathodic scan and absent in the subsequent cycles corresponds to the irreversible decomposition of organic electrolyte to form the solid-electrolyte interphase (SEI).[44] During

© 2024 The Authors. Small published by Wiley-VCH GmbH

16136829, 2024, 28, Downloaded from https://onlinelibrary.wiley.com/doi/10.1002/smll.202309321 by National Institute For, Wiley Online Library on [12/11/2024]. See the Terms and Conditions (https://onlinelibrary.wiley.com/terms-and-conditions) on Wiley Online Library for rules of use; OA articles are governed by the applicable Creative Commons License

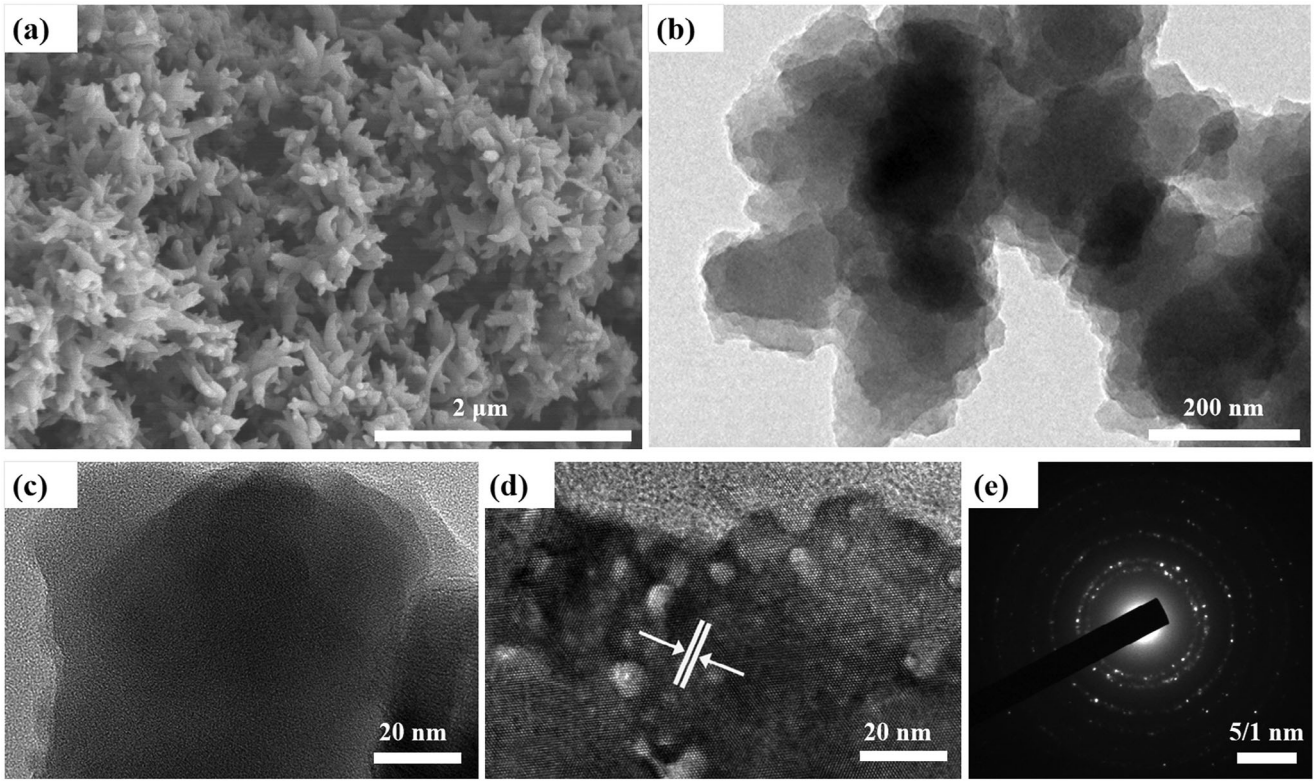

Figure 2. a) FE-SEM image, b) TEM image, c,d) high-resolution TEM image, and e) the corresponding SAED pattern of RSFP.

the anodic scan, two broad anodic peaks at 0.92–1.92 and 2.3 V correspond to the lithium-ion extraction behavior of the carbon framework, nitrogen atoms, and phenol groups in the organic framework of RSFP.[19,46] The subsequent CV curves are similar, indicating the good cycling stability of RSFP. It should be noted that the cathodic peak shifts to a higher potential from 1.47 to 1.75 V due to the emergence of C═O originating from C—O during the charge/discharge process.[45] Figure 3b shows the galvanostatic charge/discharge profiles of RSFP in the first five cycles along with the 50th, 100th, and 150th cycles. The voltage plateaus in the charge/discharge curves correspond to the redox peaks in the CV curves. The charge/discharge curves from the 2nd to 5th cycles are similar, further confirming the excellent electrochemical stability of RSFP. From the charge and discharge curves of RSFP, the initial charge/discharge capacities were calculated to be 423.2/1203.7 mAh g^{-1} with an initial coulombic efficiency (CE) of 35.16%. The large capacity loss results from the irreversible consumption of lithium ions and decomposition of organic electrolyte to form the SEI film. Figure 3c shows the enlarged galvanostatic discharge profiles of RSFP during the first five cycles along with the 50th, 100th, and 150th cycles. The observed upward potential implies the lithiation behavior of C═O derived from C—O, in accordance with the CV results (Figure 3a).

As shown in Figure 3d, the electrochemical performance of RSFP as an anode for LIBs was evaluated by a long-term cycling test, revealing a high capacity of 671.8 mAh g^{-1} after 168 cycles at 0.05 A g^{-1}. Also, the Coulombic efficiency of RSFP is low during initial cycles but rapidly approaches 100%, indicating the formation of a stable SEI layer, which is good agreement with previous studies.[19,44] Higher mass loading of RSFP was also investigated (Figure S11, Supporting Information), presenting a similar phenomenon with continuously increasing specific capacity except for a slightly lower reversible specific capacity attributed to poor organic electrolyte infiltration and slow charge transfer, which leads to a low utilization ratio of active sites and sluggish kinetics.[26,40] Remarkably, the obviously increasing capacity indicates some activation behavior by the organic framework of the cycled RSFP, leading to a greater number of redox-active sites than contained in pristine RSFP. Figure 3e shows the rate performance of RSFP, indicating reversible storage capacities of 417.2, 376, 370.5, 331, 269, 189.7, 143, and 138.6 mAh g^{-1} at current densities of 0.05, 0.1, 0.15, 0.25, 0.5, 1, 2, and 4 A g^{-1}, respectively. Notably, when the current density returns to 0.05 A g^{-1}, a reversible capacity of 498.9 mAh g^{-1} is achieved, implying the robustness of the RSFP structure. It should be noted that the reversible capacity gradually enhances after 100 cycles at 2 A g^{-1}, further confirming the activation process of RSFP. This result coincides well with the long-term cycling performance of RSFP tested at 2 A g^{-1} (Figure 3f); the gradual enhancement eventually leads to an unprecedented capacity of 946.2 mAh g^{-1} after 3500 cycles with the CE approaching 100%. Notably, during the long-term cycling test, a current density of 0.05 A g^{-1} was applied in the first 10 cycles to facilitate the infiltration of organic electrolyte into the interior of RSFP and accelerate the activation process.[46] The long-term cycled electrode measured by ex situ powder XRD shows a strong diffraction peak in the small-angle diffraction region, in good agreement with that of the pristine electrode (Figure S12, Supporting Information). Based on ex situ

© 2024 The Authors. Small published by Wiley-VCH GmbH

16136829, 2024, 28, Downloaded from https://onlinelibrary.wiley.com/doi/10.1002/smll.202309321 by National Institute For, Wiley Online Library on [12/11/2024]. See the Terms and Conditions (https://onlinelibrary.wiley.com/terms-and-conditions) on Wiley Online Library for rules of use; OA articles are governed by the applicable Creative Commons License

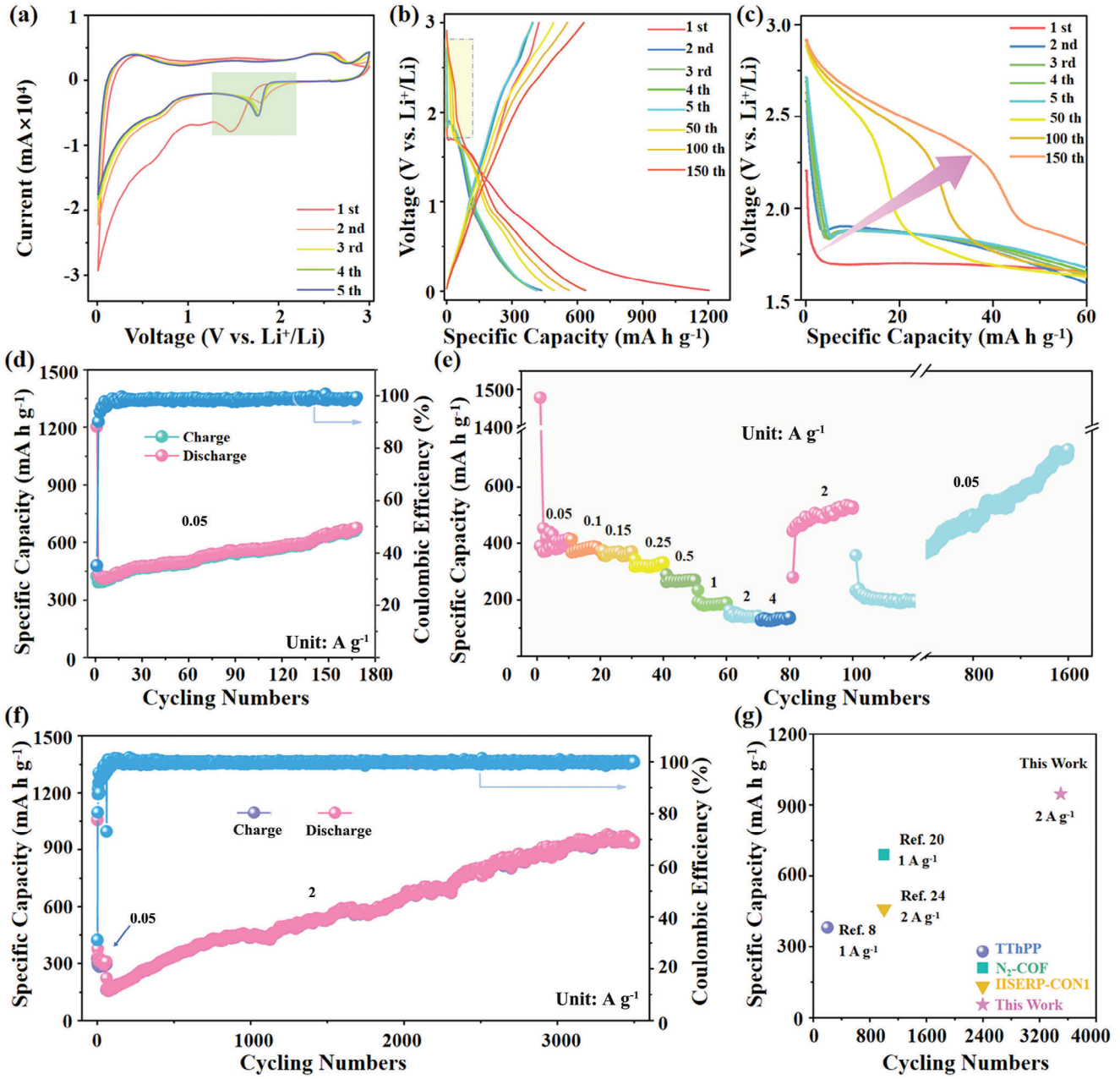

Figure 3. a) CV curves at 0.2 mV s^{-1}, b) charge/discharge curves at 0.05 A g^{-1}, c) enlarged discharge curves at 0.05 A g^{-1}, d) cycling performance at 0.05 A g^{-1}, e) rate performance at different current densities from 0.05 to 4 A g^{-1}, and f) long-term cycling performance at 2 A g^{-1} of RSFP. g) Performance comparison between RSFP and previously reported polymers.

FE-SEM observation (Figure S13, Supporting Information), the long-term cycled electrode exhibits a similar morphology to the pristine electrode, indicating the excellent electrochemical stability of RSFP. The structural evolution of the organic framework after long-term cycling was investigated by FT-IR spectroscopy (Figure S14, Supporting Information). The stretching vibration band at 1653 cm^{-1} can be ascribed to C=N in RSFP. The TGA curves of the cycled and pristine electrodes are similar (Figure S15, Supporting Information), further confirming the structural stability of organic framework after the long-term cycling performance test. The excellent electrochemical performance of RSFP as an anode material for LIBs is based on the following features: 1) the π-conjugated organic framework accelerates electron transport; 2) the polymerized organic framework with strong imine bonding improves cycling stability; 3) the well-defined pore aperture facilitates lithium-ion diffusion in the organic electrolyte; 4) the moderate specific surface area improves contact between the active electrode and electrolyte; and 5) the unique molecular architecture shortens the lithium-ion diffusion distance. Figure 3g compares the performance of RSFP with those of previously reported polymers, demonstrating the excellent durability and long-term cycling capacity of RSFP.

© 2024 The Authors. Small published by Wiley-VCH GmbH

16136829, 2024, 28, Downloaded from https://onlinelibrary.wiley.com/doi/10.1002/smll.202309321 by National Institute For, Wiley Online Library on [12/11/2024]. See the Terms and Conditions (https://onlinelibrary.wiley.com/terms-and-conditions) on Wiley Online Library for rules of use; OA articles are governed by the applicable Creative Commons License

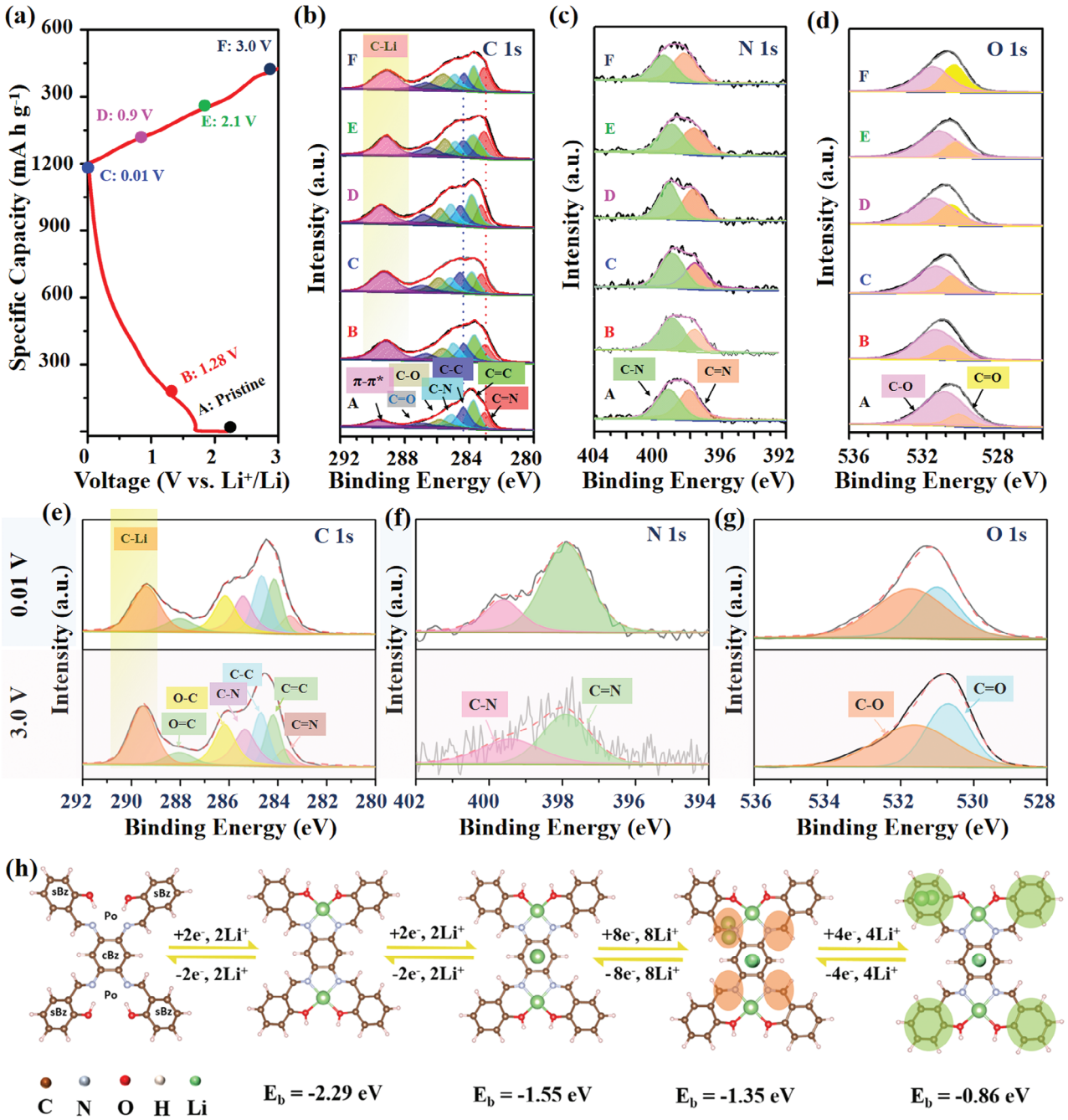

Figure 4. a) Initial charge and discharge curves of RSFP. Ex situ XPS spectra of RSFP at different charge and discharge states: b) C 1s, c) N 1s, and d) O 1s. e) C 1s, f) N 1s, and g) O 1s XPS spectra of RSFP at 0.01 and 3.0 V after long-term cycling. h) Structural evolution of RSFP during the charge/discharge process.

The corresponding volumetric energy densities were calculated and are listed in Table S2 (Supporting Information). RSFP displays an excellent volumetric energy density and outperforms other previously reported electrode materials, further demonstrating that RSFP is an ideal next-generation organic anode material for LIBs.

The lithium insertion/extraction mechanism of RSFP was investigated by ex situ XPS at different states of lithiation/delithiation (**Figure** 4a). As shown in Figure 4b, the high-resolution C 1s spectra of RSFP can be deconvoluted into six peaks at 283.5, 284.4, 285.1, 285.8, 286.5, and 287.7 eV, which correspond respectively to the C═N, C═C, C─C, C─N, C─O, and C═O bonding states.[8,26] Peaks corresponding to the C─C/C═C groups in the benzene rings of RSFP move to higher binding energy during the discharge process and return to lower binding energy during the charging process. A new peak appearing

© 2024 The Authors. Small published by Wiley-VCH GmbH

16136829, 2024, 28, Downloaded from https://onlinelibrary.wiley.com/doi/10.1002/smll.202309321 by National Institute For, Wiley Online Library on [12/11/2024]. See the Terms and Conditions (https://onlinelibrary.wiley.com/terms-and-conditions) on Wiley Online Library for rules of use; OA articles are governed by the applicable Creative Commons License

at 289.5 eV is assigned to the formation of C-Li,[26] indicating that lithium insertion/extraction also occurs at the C_6 aromatic benzene rings. As shown in Figure 4c, the N 1s spectra of RSFP can be deconvoluted into two peaks at 397.9 and 399.2 eV, corresponding to C═N and C—N, respectively.[38] The fitted peak of C═N shifts to a lower binding energy due to the formation of N-Li during the lithiation process[47] and returns to its initial binding energy during the delithiation process, indicating the lithiation/delithiation behavior of C═N in the organic framework. The high-resolution O 1s spectra shown in Figure 4d contain two fitted peaks at 531.74 and 530.75 eV, which are respectively attributed to the C—O and C═O groups. Notably, these peaks shift to higher binding energy during the lithiation process and return to the initial binding energies during the delithiation process, revealing that C—O and C═O actively participate in lithium storage. The intensity of the C-Li peak increases after 3500 cycles, indicating the accommodation of more lithium ions by the activated benzene rings of the organic framework of RSFP (Figure 4e). Meanwhile, the intensities of the C—N (Figure 4f) and C—O (Figure 4g) peaks decrease, while those of the C═N (Figure 4f) and C═O (Figure 4g) peaks increase continuously during the lithiation/delithiation process as the number of cycles increases. This suggests the transformation of C—N and C—O to C═N and C═O, respectively, in the organic framework of RSFP triggered by lithiation/delithiation behavior based on the reversibility of these active sites. These results confirm that the C═N, C—O, and C═O groups along with the C_6 benzene rings in the organic framework of RSFP are beneficial for reversible lithium-ion insertion/extraction and are responsible for the superior electrochemical performance of RSFP.

The structural evolution of RSFP during the lithiation/delithiation process was further verified through DFT calculations based on an isolated RSFP unit. As shown in Figure 4h, four possible binding sites of lithium ions were identified through structural optimization: the salen group with two O and two N atoms (Po), aromatic benzene rings located in the center of four N atoms (cBz), nitrogen atoms (N), and benzene rings not associated with N atoms (sBz). According to the DFT results, the lowest ΔE_b of −2.29 eV was obtained for Li@Po, suggesting the strongest binding at those sites. Notably, lithium-ion diffusion and delithiation can be arrested or obstructed by such strong binding. This binding event is probably responsible for the irreversible electrochemical reactions and the large loss of capacity observed in the initial charge/discharge process. Subsequently, lithium ions can be adsorbed at either cBz or N atoms, which have strong binding energies of −1.55 and −1.35 eV, respectively. These values are similar to those for lithium-ion accommodation in carbon-based electrode materials,[48–50] indicating that both aromatic benzene and C═N participate in the lithiation/delithiation processes. The results reveal that each cBz and N site can adsorb two lithium ions. Given that there are four N atoms and one cBZ group in each unit, 10 lithium ions can be adsorbed at each RSFP unit. The theoretical capacity can then be calculated using Equation (1):

$$\text{Theoretical capacity} = (n \times F) / (3.6 \times M) \quad (1)$$

where n is the number of lithium ions adsorbed on RSFP, F is the Faraday constant, and M is the molar mass of each RSFP unit (398 g mol^{-1}). Based on this, the theoretical capacity is 670.1 mA h g^{-1}, which is close to the measured capacity of 671.8 mAh g^{-1} at 0.05 A g^{-1}. In addition, the ΔE_b value for Li@sBz is the largest (−0.86 eV), indicative of the weakest binding strength, implying that a high current density is required to enable lithiation. Considering the periodic structure of RSFP (Figure 1a), two sBz sites in each RSFP unit are adopted. As a result, four lithium ions can be adsorbed since each sBz site can host two lithium ions. Thus, a total of 14 Li atoms can be adsorbed in the RSFP unit if the charge current density is sufficiently high. In this case, the corresponding theoretical capacity is 938.2 mAh g^{-1}. This value is in good agreement with the measured capacity of 946.2 mAh g^{-1} after 3500 cycles at 2 A g^{-1}. The above results confirm that a 14-electron redox reaction occurs at the C═N, C—O, C═O, and benzene ring sites in the organic framework during the charge/discharge process.

A possible lithium storage scenario for RSFP as an anode material for LIBs is illustrated in **Figure 5**. The enlarged structural units of RSFP in the organic framework offer multiple redox-active centers (C—O, C═N, and benzene rings) during the initial discharge process; these groups should be responsible for the lithiation behavior corresponding to the cathodic peaks observed at 1.75, 1.47, and 0.63 V, respectively, in the CV curves (Figure 3a). The redox-active centers of benzene rings and C═N react, as indicated by the broad oxidation peak at 0.92–1.92 V, with partial -O-Li transforming into C═O occurring at 2.1–2.7 V (Figure 3a). In subsequent lithiation/delithiation processes, the accessible redox-active centers of C═N, C—O, C═O, and benzene rings endow the unique framework of RSFP with superior electrochemical performance.

For an in-depth study of the capacitive behavior of RSFP, the reaction kinetics were evaluated by CV. **Figure 6**a shows the CV curves measured at scan rates ranging from 0.2 to 1.0 mV s^{-1}. Normally, the relationship between the peak current (i) and scan rate (v) can be expressed by Equations (2) and (3)[51]:

$$i = av^b \quad (2)$$

$$\log(i) = b\log(v) + \log(a) \quad (3)$$

where a and b are empirical parameters. According to literature report,[52] the b value can be obtained from the slope of the line based on Equation (3), which is derived from Equation (2). A value of b approaching 0.5 signifies diffusion-controlled behavior, while a b value closer to 1.0 indicates capacitive performance. In this work, the b values of peaks 1, 2, and 3 were calculated as 0.99, 0.82, and 0.91, respectively (Figure 6b), implying the coexistence of capacitive and diffusive behaviors in RSFP during the charge/discharge process. The capacitive contribution to total capacity can be quantified by Equation (4)[53]:

$$i_{(V)} = k_1 v + k_2 v^{0.5} \quad (4)$$

$$i_{(V)}/v^{0.5} = k_1 v^{0.5} + k_2 \quad (5)$$

where k_1 and k_2 are constants that can be obtained from Equation (5), which is derived from Equation (4), and $k_1 v$ and $k_2 v^{0.5}$ represent the capacitive and diffusion-controlled contributions, respectively. As shown in Figure 6c, the capacitive contributions

© 2024 The Authors. Small published by Wiley-VCH GmbH

16136829, 2024, 28, Downloaded from https://onlinelibrary.wiley.com/doi/10.1002/smll.202309321 by National Institute For, Wiley Online Library on [12/11/2024]. See the Terms and Conditions (https://onlinelibrary.wiley.com/terms-and-conditions) on Wiley Online Library for rules of use; OA articles are governed by the applicable Creative Commons License

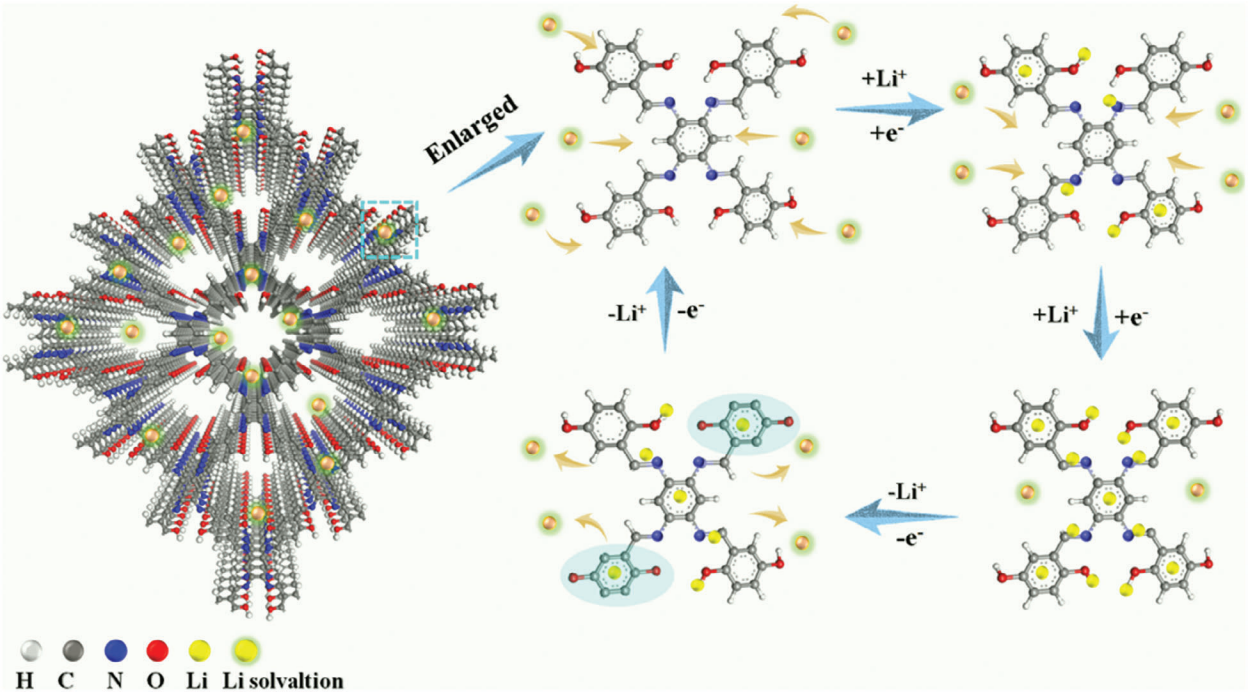

Figure 5. Schematic illustration of the lithiation and delithiation mechanism of RSFP as an anode for LIBs.

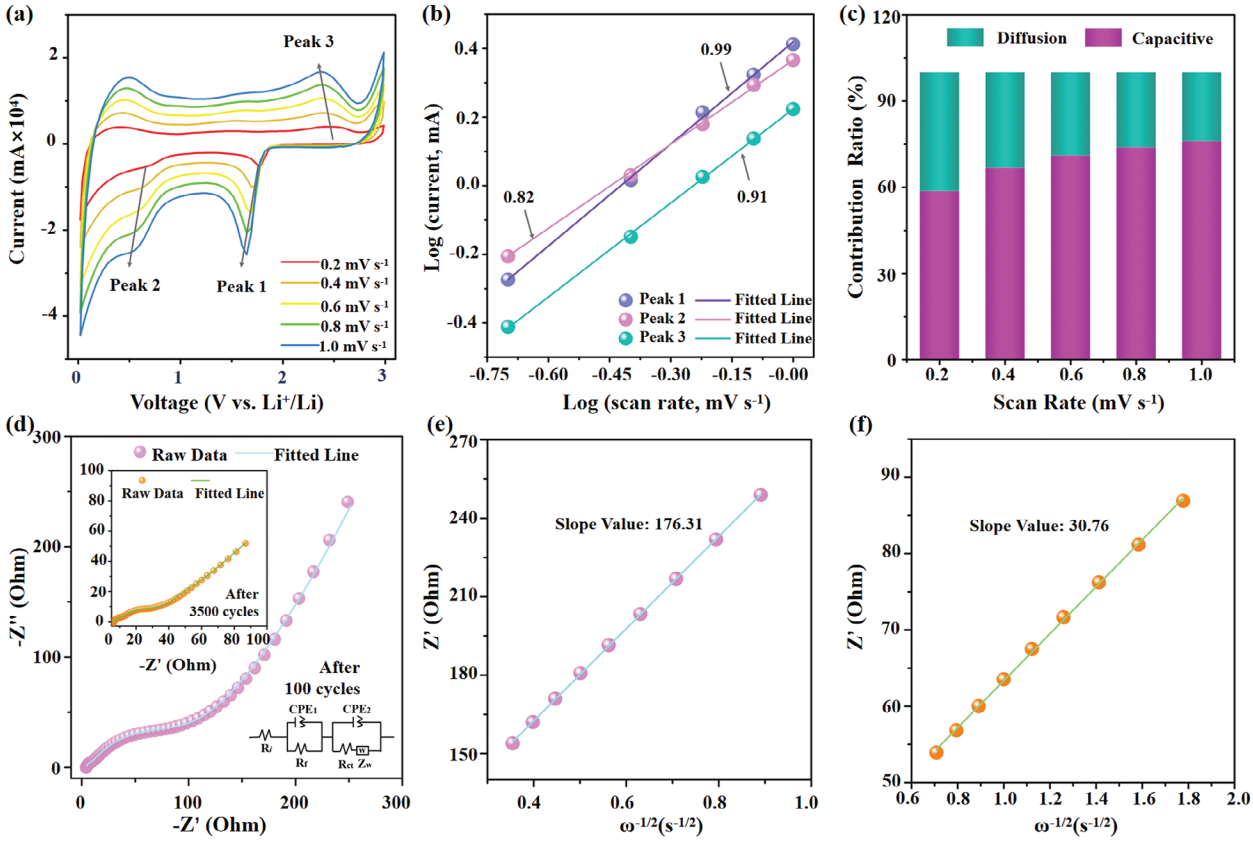

Figure 6. a) CV curves of RSFP at scan rates of 0.2-1.0 mV s^{-1}. b) Values of b calculated based on the relationship between log(i) and log(v) for different redox peaks. c) Contribution ratios of capacitive and diffusion-controlled behaviors at various scan rates. d) Nyquist plot of RSFP after 100 cycles at 2 A g^{-1} (inset shows the Nyquist plot of RSFP after 3500 cycles at 2 A g^{-1} and the equivalent circuit model). Plots of Z' versus the inverse square root of angular frequency (ω) for e) pristine RSFP and f) RSFP after long-term cycling.

© 2024 The Authors. Small published by Wiley-VCH GmbH

16136829, 2024, 28, Downloaded from https://onlinelibrary.wiley.com/doi/10.1002/smll.202309321 by National Institute For, Wiley Online Library on [12/11/2024]. See the Terms and Conditions (https://onlinelibrary.wiley.com/terms-and-conditions) on Wiley Online Library for rules of use; OA articles are governed by the applicable Creative Commons License

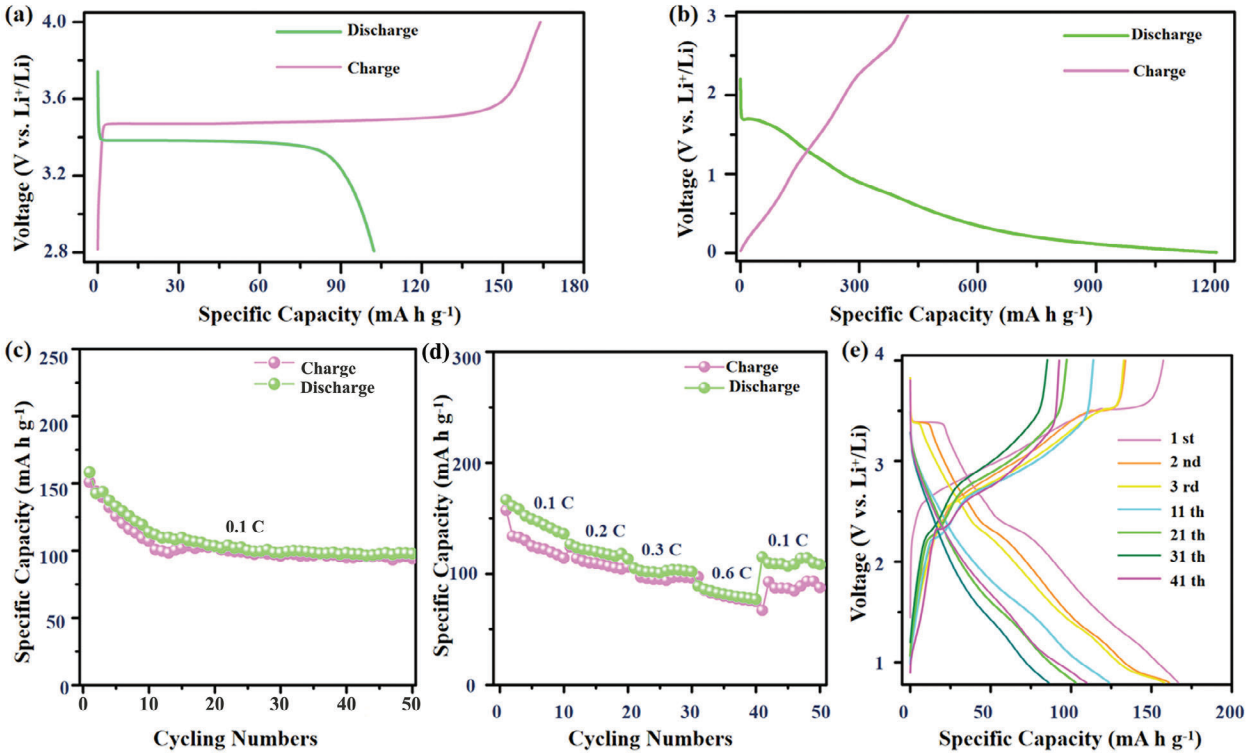

Figure 7. Charge/discharge curves of a) the Li/LiFePO$_4$ half battery at 2.8-4.0 V and b) the Li/RSFP half battery at 0.01–3.0 V. Electrochemical performances of full cells with LiFePO4 as cathode and RSFP as anode: c) cycling performance at 0.1 C, d) rate performance, and e) charge/discharge curves at different current densities from 0.1 to 0.6 C.

were calculated to be 58.7%, 66.7%, 71.0%, 73.9%, and 76.0% at 0.2, 0.4, 0.6, 0.8, and 1.0 mV s^{-1}, respectively, revealing that capacitive behavior dominates lithium-ion storage, which is beneficial for the long-term cycling performance of RSFP. Subsequently, RSFP was subjected to electrochemical impedance spectroscopy (EIS) measurements in the frequency range 10 to 100 kHz after 100 and 3500 cycles at 2 A g^{-1} (Figure 6d).

Based on the Nyquist plots obtained for RSFP, the corresponding equivalent circuit model was constructed (inset of Figure 6d). The circuit consists of a depressed semicircle at high frequency related to the SEI layer (R_f) resistance, a large semicircle at intermediate frequency associated with the charge transfer resistance (R_{ct}), and an inclined line at low frequency corresponding to Warburg diffusion resistance (Z_w). The fitted R_{ct} values of RSFP after 100 and 3500 cycles are 110 and 21.4 Ω, respectively, indicating that the charge transfer ability is enhanced as the cycle number increases. This feature is beneficial for electrochemical performance, in accordance with the activation behavior of RSFP during the charge/discharge process. The lithium-ion diffusion coefficient (D_{Li+}) estimated for the Li$^+$ diffusion kinetics of RSFP can be calculated using EIS according to Equation (6)[54,55,29]:

$$D_{Li+} = 0.5 \times \left(RT/AF^2C\sigma_w\right)^2 \quad (6)$$

where R is the gas constant (8.314 J mol^{-1} k^{-1}), T is the absolute temperature (298.5 K), A is the surface area of the electrode (1.538 cm^2), F is the Faraday constant (96 485 C mol^{-1}), C is the concentration of lithium ions (1.0 × 10^{-3} mol cm^{-3}), and σ_w is the Warburg factor obtained from the line slope of the Nyquist plot in the low-frequency region (Figure 6e,f) based on Equation (7)[56,57]:

$$Z = R_e + R_{ct} + \sigma_w\omega^{-1/2} \quad (7)$$

where R_e represents the resistance between the electrode and electrolyte, and ω is the angular frequency in altering-current impedance. The σ_w values of pristine RSFP and RSFP after 3500 cycles were calculated to be 176.31 and 30.76 s$^{-1/2}$, respectively, with the corresponding D_{Li+} values being 4.82 × 10^{-13} and 1.58 × 10^{-11} cm^2 s^{-1}, respectively. The diffusion coefficients shown in Table S3 (Supporting Information) highlight the superior Li$^+$ diffusion kinetics in RSFP compared to previously reported polymers. The increased D_{Li+} of this electrode after long-term cycling indicates rapid lithium-ion diffusion in the solid phase of the RSFP, which can be ascribed to its active organic framework that facilitates Li$^+$ diffusion.

To evaluate the practical application potential of RSFP, full cells were assembled with pre-lithiated RSFP as anode and LiFePO$_4$ as cathode in the voltage range from 0.8 to 4.0 V. This voltage window is selected based on the charge/discharge curves of the Li/LiFePO$_4$ half battery in the voltage range of 2.8 to 4.0 V (**Figure 7a**) and the charge/discharge curves of the Li/RSFP half battery in the voltage range of 0.01 to 3.0 V (Figure 7b). As shown in Figure 7c, the full cell displays a superior reversible capacity of 97.7 mAh g^{-1} after 50 cycles at 0.1 C (1 C = 170 mA g^{-1}). In

© 2024 The Authors. Small published by Wiley-VCH GmbH

16136829, 2024, 28, Downloaded from https://onlinelibrary.wiley.com/doi/10.1002/smll.202309321 by National Institute For, Wiley Online Library on [12/11/2024]. See the Terms and Conditions (https://onlinelibrary.wiley.com/terms-and-conditions) on Wiley Online Library for rules of use; OA articles are governed by the applicable Creative Commons License

comparison to the above performance, the full battery with pristine RSFP as anode (Figure S16, Supporting Information) delivers inferior cycling performance due to the persistent loss of lithium ions. Figure 7d shows the rate performance with reversible storage capacities of 149.3, 120.1, 100.7, 81.7, and 106.8 mAh g^{-1} at current densities of 0.1, 0.2, 0.3, 0.6, and 0.1 C, respectively. Notably, when the current density returns to 0.1 C, a reversible capacity of 106.8 mAh g^{-1} is achieved, implying the robustness of the electrode structure. Figure 7e shows the charge/discharge profiles of the full cell at different current densities in the first three cycles along with the 11th, 21st, 31st, and 41st cycles. The charge/discharge curves from the first to third cycles almost overlap, confirming the excellent electrochemical stability of the full cell. From the charge and discharge curves of the full cell, the initial discharge/charge capacities were calculated to be 166.6/157.4 mAh g^{-1} with an initial Coulombic efficiency (CE) of 105.8%. It should be noted that CE exceeding 100% can be explained by pre-lithiated RSFP providing sufficient lithium ions for accommodation at its increasingly abundant active centers and the consumption of organic electrolyte.[58,59]

3. Conclusion

A multi-redox-active RSFP has been synthesized using a facile solvothermal approach based on Schiff base reaction. When used as an anode material for LIBs, RSFP delivers a high reversible capacity of 671.8 mAh g^{-1} at 0.05 A g^{-1} after 168 cycles, a lithium storage performance that is gradually enhanced during long-term cycling, and an impressive reversible capacity of 946.2 mAh g^{-1} after 3500 cycles at 2 A g^{-1}. The superior electrochemical performance is based on: (1) multiple accessible redox centers acting as binding sites for lithium ions, (2) a π-conjugated organic framework which improves electron transport, (3) a polymerized organic framework with strong imine bonding which improves structural stability, (4) a large pore aperture facilitating lithium-ion diffusion in organic electrolyte, (5) a specific surface area sufficient to optimize contact between the active electrode and electrolyte, and (6) a unique architecture, which shortens the distance required for lithium-ion diffusion. Structural evolution of RSFP was also successfully studied ex-situ by using XPS, confirming the presence of multiple redox-active sites (C═N, C—O, C═O, and benzene rings) in the organic framework. Furthermore, the strong and weak binding of lithium ions at active sites correspond to superior theoretical capacities of 670.1 and 938.2 mAh g^{-1}, respectively, and DFT calculations confirm that the lithiation/delithiation process of RSFP involves a 14-electron redox reaction. The high-performance RSFP material reported in this work is a promising organic electrode for energy storage applications.

Supporting Information

Supporting Information is available from the Wiley Online Library or from the author.

Acknowledgements

The authors appreciate the financial support from the Shanghai Domestic Science and Technology Cooperation Project (21015801000), the Project of Ningxia Key R&D Plan (2021BEE03006), the UQ-Yonsei International Research Project, and the JST-ERATO Yamauchi Materials Space-Tectonics Project (Grant Number: JPMJER2003). The Instrumental Analysis Center of Shanghai Jiao Tong University is also acknowledged for some of the measurements. This work used the Queensland node of the NCRIS-enabled Australian National Fabrication Facility (ANFF). Y.B. and S.M.A. appreciate the Distinguished Scientist Fellowship Program (DSFP) at King Saud University, Riyadh, Kingdom of Saudi Arabia for the financial support.

Open access publishing facilitated by The University of Queensland, as part of the Wiley - The University of Queensland agreement via the Council of Australian University Librarians.

Conflict of Interest

The authors declare no conflict of interest.

Data Availability Statement

The data that support the findings of this study are available from the corresponding author upon reasonable request.

Keywords

lithium-ion storage, redox chemistry, redox-active framework polymer, storage mechanism, structural evolution

Received: October 15, 2023
Revised: January 12, 2024
Published online: March 25, 2024

[1] F. Chen, L. Wu, Z. Zhou, J. Ju, Z. Zhao, M. Zhong, T. Kuang, *Chinese. Chem. Lett.* **2019**, *3*, 197.
[2] W. Chen, Y.-F. Gong, J.-H. Liu, *Chinese. Chem. Lett.* **2017**, *28*, 709.
[3] S. Jin, J. Liang, D. Mu, T. Lin, Y. Tian, J. Zhang, Y. Wang, M. Chen, Q. Shi, C. Dai, *SusMat.* **2023**, *3*, 362378.
[4] J. Xie, J. Li, X. Li, H. Lei, W. Zhuo, X. Li, G. Hong, N. Hui Kwun, L. Pan, W. Mai, *CCS Chem.* **2020**, *3*, 791.
[5] J. Lian, Y. Wu, Y. Guo, Z. Zhao, Q. Zhang, Y. Hou, L. Chen, B. Lu, X. Pan, Z. Ye, J. Lu, *Chinese. Chem. Lett.* **2022**, *33*, 3931.
[6] S. Chen, C. Yu, S. Chen, L. Peng, C. Liao, C. Wei, Z. Wu, S. Cheng, J. Xie, *Chinese. Chem. Lett.* **2022**, *33*, 4635.
[7] X. Chen, Y. Li, L. Wang, Y. Xu, A. Nie, Q. Li, F. Wu, W. Sun, X. Zhang, R. Vajtai, P. M. Ajayan, L. Chen, Y. Wang, *Adv. Mater.* **2019**, *31*, 1901640.
[8] B. C. Patra, S. Khilari, L. Satyanarayana, D. Pradhan, A. Bhaumik, *Chem. Commun.* **2016**, *52*, 7592.
[9] L. Zhang, H. B. Wu, X. W. Lou, *Adv. Energy Mater.* **2014**, *4*, 1300958.
[10] S. Haldar, K. Roy, R. Kushwaha, S. Ogale, R. Vaidhyanathan, *Adv. Energy Mater.* **2019**, *9*, 1902428.
[11] G. Wang, N. Chandrasekhar, B. P. Biswal, D. Becker, S. Paasch, E. Brunner, M. Addicoat, M. Yu, R. Berger, X. Feng, *Adv. Mater.* **2019**, *3*, 1901478.
[12] Q. Zhao, Z. Zhu, J. Chen, *Adv. Mater.* **2017**, *29*, 1607007.
[13] S. Lee, G. Kwon, K. Ku, K. Yoon, S.-K. Jung, H.-D. Lim, K. Kang, *Adv. Mater.* **2018**, *30*, 1704682.
[14] Y. Wang, Y. Ding, L. Pan, Y. Shi, Z. Yue, Y. Shi, G. Yu, *Nano Lett.* **2016**, *16*, 3329.
[15] R. Shi, C. Han, H. Duan, L. Xu, D. Zhou, H. Li, J. Li, F. Kang, B. Li, G. Wang, *Adv. Energy Mater.* **2018**, *8*, 1802088.
[16] L. Zhou, S. Jo, M. Park, L. Fang, K. Zhang, Y. Fan, Z. Hao, Y. M. Kang, *Adv. Energy Mater.* **2021**, *11*, 2003054.

© 2024 The Authors. Small published by Wiley-VCH GmbH

16136829, 2024, 28, Downloaded from https://onlinelibrary.wiley.com/doi/10.1002/smll.202309321 by National Institute For, Wiley Online Library on [12/11/2024]. See the Terms and Conditions (https://onlinelibrary.wiley.com/terms-and-conditions) on Wiley Online Library for rules of use; OA articles are governed by the applicable Creative Commons License

[17] K. C. Ranjeesh, R. Illathvalappil, S. D. Veer, J. Peter, V. C. Wakchaure, Goudappagouda, K. V. Raj, S. Kurungot, S. S. Babu, *J. Am. Chem. Soc.* **2019**, *141*, 14950.
[18] Q. Li, D. Li, H. Wang, H.-g. Wang, Y. Li, Z. Si, Q. Duan, *ACS Appl. Mater. Interfaces* **2019**, *11*, 28801.
[19] J. Wu, X. Rui, C. Wang, W.-B. Pei, R. Lau, Q. Yan, Q. Zhang, *Adv. Energy Mater.* **2015**, *5*, 1402189.
[20] L. Bai, Q. Gao, Y. Zhao, *J. Mater. Chem. A* **2016**, *4*, 14106.
[21] G. Q. Xiaoyan Han, J. Sun, T. Sun, *Angew. Chem., Int. Ed.* **2012**, *5*, 5147.
[22] Y. Zhang, S. N. Riduan, J. Wang, *Chem.-Eur. J.* **2017**, *23*, 16419.
[23] Y. Chen, H. Li, M. Tang, S. Zhuo, Y. Wu, E. Wang, S. Wang, C. Wang, W. Hu, *J. Mater. Chem. A* **2019**, *7*, 20891.
[24] S. Haldar, K. Roy, S. Nandi, D. Chakraborty, D. Puthusseri, Y. Gawli, S. Ogale, R. Vaidhyanathan, *Adv. Energy Mater.* **2018**, *8*, 1702170.
[25] P. Das, S. K. Mandal, *Chem. Mater.* **2019**, *31*, 1584.
[26] Z. Lei, Q. Yang, Y. Xu, S. Guo, W. Sun, H. Liu, L. P. Lv, Y. Zhang, Y. Wang, *Nat. Commun.* **2018**, *9*, 576.
[27] T. Li, W.-D. Zhang, Y. Liu, Y. Li, C. Cheng, H. Zhu, X. Yan, Z. Li, Z.-G. Gu, *J. Mater. Chem. A* **2019**, *7*, 19676.
[28] L. H. Li, X. L. Feng, X. H. Cui, Y. X. Ma, S. Y. Ding, W. Wang, *J. Am. Chem. Soc.* **2017**, *139*, 6042.
[29] X. Zhang, L. Han, J. Li, T. Lu, J. Li, G. Zhu, L. Pan, *J. Mater. Sci. Technol.* **2022**, *97*, 156.
[30] J. Wang, L. Si, Q. Wei, X. Hong, S. Cai, Y. Cai, *ACS Appl. Nano Mater.* **2018**, *1*, 132.
[31] X. Han, Q. Xia, J. Huang, Y. Liu, C. Tan, Y. Cui, *J. Am. Chem. Soc.* **2017**, *139*, 8693.
[32] B. P. Biswal, S. Chandra, S. Kandambeth, B. Lukose, T. Heine, R. Banerjeet, *J. Am. Chem. Soc.* **2013**, *135*, 5328.
[33] S. Bhunia, S. K. Das, R. Jana, S. C. Peter, S. Bhattacharya, M. Addicoat, A. Bhaumik, A. Pradhan, *ACS Appl. Mater. Interfaces* **2017**, *9*, 23843.
[34] H. Li, X. Feng, P. Shao, J. Chen, C. Li, S. Jayakumar, Q. Yang, *J. Mater. Chem. A* **2019**, *7*, 5482.
[35] H. Guo, J. Wang, Q. Fang, Y. Zhao, S. Gu, J. Zheng, Y. Yan, *CrystEngComm* **2017**, *19*, 4905.
[36] A. Moya, M. Hernando-Perez, M. Perez-Illana, C. San Martin, J. Gomez-Herrero, J. Aleman, R. Mas-Balleste, P. J. de Pablo, *Nanoscale* **2020**, *12*, 1128.
[37] I. Berlanga, M. L. Ruiz-Gonzalez, J. M. Gonzalez-Calbet, J. L. Fierro, R. Mas-Balleste, F. Zamora, *Small* **2011**, *7*, 1207.
[38] B. C. Patra, S. K. Das, A. Ghosh, A. Raj K, P. Moitra, M. Addicoat, S. Mitra, A. Bhaumik, S. Bhattacharya, A. Pradhan, *J. Mater. Chem. A* **2018**, *6*, 16655.
[39] H. Yang, Y. Du, S. Wan, G. D. Trahan, Y. Jin, W. Zhang, *Chem. Sci.* **2015**, *6*, 4049.
[40] M. Tang, S. Zhu, Z. Liu, C. Jiang, Y. Wu, H. Li, B. Wang, E. Wang, J. Ma, C. Wang, *Chem* **2018**, *4*, 2600.
[41] P. Wei, M. Qi, Z. Wang, S. Ding, W. Yu, Q. Liu, L. Wang, H. Wang, W. An, W. Wang, *J. Am. Chem. Soc.* **2018**, *140*, 4623.
[42] Z.-Q. Lin, J. Xie, B.-W. Zhang, J.-W. Li, J. Weng, R.-B. Song, X. Huang, H. Zhang, H. Li, Y. Liu, Z. J. Xu, W. Huang, Q. Zhang, *Nano Energy* **2017**, *41*, 117.
[43] Y. Ma, J. He, Z. Kou, A. M. Elshahawy, Y. Hu, C. Guan, X. Li, J. Wang, *Adv. Mater. Interfaces* **2018**, *5*, 1800222.
[44] J. Wu, X. Rui, G. Long, W. Chen, Q. Yan, Q. Zhang, *Angew. Chem., Int. Ed.* **2015**, *54*, 7354.
[45] K. Cao, L. Jiao, H. Liu, Y. Liu, Y. Wang, Z. Guo, H. Yuan, *Adv. Energy Mater.* **2015**, *5*, 1401421.
[46] C. Li, X. Lou, M. Shen, X. Hu, W. Yan, Y. Zou, W. Tong, B. Hu, *Energy Storage Mater.* **2017**, *7*, 195.
[47] C. Yan, Y. X. Yao, X. Chen, X. B. Cheng, X. Q. Zhang, J. Q. Huang, Q. Zhang, *Angew. Chem., Int. Ed.* **2018**, *57*, 14055.
[48] Q. Sun, P. Jena, Q. Wang, M. Marquez, *J. Am. Chem. Soc.* **2006**, *128*, 9741.
[49] B. Jang, J. Koo, M. Park, H. Lee, J. Nam, Y. Kwon, H. Lee, *Appl. Phys. Lett.* **2013**, *103*, 263904.
[50] K. T. Chan, J. B. Neaton, M. L. Cohen, *Phys. Rev. B* **2008**, *77*, 235430.
[51] J. Li, N. Zhuang, J. Xie, X. Li, W. Zhuo, H. Wang, J. B. Na, X. Li, Y. Yamauchi, W. Mai, *Adv. Energy Mater.* **2020**, *10*, 1903455.
[52] X. Zhang, J. Li, J. Li, L. Han, T. Lu, X. Zhang, G. Zhu, L. Pan, *Chem. Eng. J.* **2020**, *385*, 123394.
[53] J. Xie, X. Li, H. Lai, Z. Zhao, J. Li, W. Zhang, W. Xie, Y. Liu, W. Mai, *Angew. Chem., Int. Ed.* **2019**, *58*, 14740.
[54] Q. Pan, S. Chen, C. Wu, Z. Zhang, Z. Li, Y. Zhao, *ACS Appl. Mater. Interfaces* **2019**, *11*, 46070.
[55] R. Chen, J. Zhao, Z. Yu, M. Cong, Y. Wang, M. Wang, G. Li, Z. Li, Y. Zhao, *ACS Appl. Mater. Interfaces* **2022**, *15*, 830.
[56] S. Wang, Q. Wang, P. Shao, et al., *J. Am. Chem. Soc.* **2017**, *139*, 4258.
[57] X. Zhang, Z. Ni, X. Bai, H. Shen, Z. Wang, C. Wei, K. Tian, B. Xi, S. Xiong, J. Feng, *Adv. Energy Mater.* **2023**, *13*, 2301349.
[58] J. Lee, D. Jin, J. Y. Kim, Y. Roh, H. Lee, S. H. Kang, J. Choi, T. Jo, Y.-G. Lee, Y. M. Lee, *Adv. Energy Mater.* **2023**, *13*, 2300172.
[59] X. Chang, M. Fan, B. Yuan, C.-F. Gu, W.-H. He, C. Li, X.-X. Feng, S. Xin, Q. Meng, L.-J. Wan, Y.-G. Guo, *Angew.Chem., Int. Ed.* **2023**, *62*, e202310435.

© 2024 The Authors. Small published by Wiley-VCH GmbH

16136829, 2024, 28, Downloaded from https://onlinelibrary.wiley.com/doi/10.1002/smll.202309321 by National Institute For, Wiley Online Library on [12/11/2024]. See the Terms and Conditions (https://onlinelibrary.wiley.com/terms-and-conditions) on Wiley Online Library for rules of use; OA articles are governed by the applicable Creative Commons License